Anomalous Hall Effect in 2D Dirac Materials

Manuel Offidani and Aires Ferreira[*]
Department of Physics, University of York, York YO10 5DD, United Kingdom

(Received 24 January 2018; revised manuscript received 14 August 2018; published 17 September 2018)

We present a unified theory of charge carrier transport in 2D Dirac systems with broken mirror inversion and time-reversal symmetries (e.g., as realized in ferromagnetic graphene). We find that the entanglement between spin and pseudospin SU(2) degrees of freedom stemming from spin-orbit effects leads to a distinctive gate voltage dependence (change of sign) of the anomalous Hall conductivity approaching the topological gap, which remains robust against impurity scattering and thus is a smoking gun for magnetized 2D Dirac fermions. Furthermore, we unveil a robust skew scattering mechanism, modulated by the spin texture of the energy bands, which causes a net spin accumulation at the sample boundaries even for spin-transparent disorder. The newly unveiled extrinsic spin Hall effect is readily tunable by a gate voltage and opens novel opportunities for the control of spin currents in 2D ferromagnetic materials.

DOI: 10.1103/PhysRevLett.121.126802

Ferromagnetic order in two-dimensional (2D) crystals is of great significance for fundamental studies and applications in spintronics. Recent experiments have revealed that intrinsic ferromagnetism occurs in 2D crystals of $\mathrm{Cr_2Ge_2Te_6}$ [1] and $\mathrm{CrI_3}$ [2], while graphene and group-VI dichalcogenide monolayers acquire large exchange splitting when integrated with nanomagnets [3–9].

Different from bulk compounds, the electronic states of atomically thin layers can be dramatically affected by short-range magnetic interactions, opening up a new arena for studies of emergent spin-dependent phenomena [10–14]. In this regard, graphene and other 2D materials with multiple internal degrees of freedom offer particularly promising perspectives. The anomalous Hall effect (AHE) recently observed in graphene/yttrium iron garnet heterostructures indicates that interface-induced magnetic exchange coupling (MEC) is accompanied by a sizable Bychov-Rashba effect [4,5]. The breaking of inversion symmetry in a honeycomb layer couples different SU(2) subspaces (spin and sublattice) [15] and can drive the ferromagnetic 2D Dirac system through a topological phase transition to a Chern insulator when the chemical potential is tuned inside the gap [11,16,17]. This system is predicted to exhibit the quantum anomalous Hall effect (QAHE), with transverse conductivity $\sigma_{\mathrm{AH}} = 2e^2/h$ [11]. However, much less is known about the *nonquantized* regime at finite carrier density. The latter is the current experimental accessible regime [4,5]. Beyond the non-quantized part of the intrinsic contribution, the presence of a Fermi surface makes the transverse (anomalous Hall) conductivity depend nontrivially on spin-dependent scattering due to pseudospin-spin coupling [18–21]. Moreover, in ultraclean heterostructures, the MEC and spin-orbit coupling (SOC) energy scales can easily reach the disorder-induced broadening [22–24], thus questioning the use of standard approaches where SOC is treated as a weak perturbation.

In this Letter, we report an accurate theoretical study of charge and spin transport in magnetized 2D Dirac systems by considering the effects of strong MEC and SOC *non-perturbatively* in the presence of dilute random impurities. Our theory is valid for both weak (Born) and strong (unitary) potential scattering and accounts for intervalley processes from point defects. We find that the out-of-plane component of the noncollinear spin texture $\mathbf{S}_{\mu\nu\mathbf{k}}$ [with $\mu(\nu) = \pm 1$ pseudospin (spin chirality); Figure 1] activates a robust skew scattering mechanism, which determines the behavior of leading Fermi surface contributions to the transverse transport coefficients. The $\mathbf{k}$ modulation of the spin polarization manifests into a ubiquitous change of sign in the charge Hall conductivity as the Fermi level approaches the majority spin band edge, which, as we argue below, is a forerunner of the elusive QAHE [4,5,25]. Second, we predict that scattered electron waves with opposite polarization (e.g., from within the "Mexican hat" with $S^z_{\mathbf{k}_\pm} \gtrless 0$; Figure 1) have different transverse cross sections leading to net spin Hall current in the bulk [26]. Such a spin Hall effect (SHE) in a 2D Dirac system with broken time-reversal symmetry can be seen as the reciprocal of the inverse spin Hall effect discovered recently in ferromagnets [27–29]. The common stem of AHE and SHE implies the change of sign reveals likewise in the spin Hall response, unveiling the possibility of reversing the spin accumulation at the sample boundaries by gate voltage. The sign-change feature is preserved when adding the Berry curvature-dependent contributions to the AHE and SHE over a wide range of parameters in samples with high mobility.

Model.—The low-energy Hamiltonian reads (we use natural units $e \equiv 1 \equiv \hbar$, unless stated otherwise)

$$H = v\tau_z \mathbf{\Sigma}\cdot\mathbf{p} + \delta s_z + \lambda\tau_z(\Sigma_x s_y - \Sigma_y s_x) + V(\mathbf{x}), \quad (1)$$

where v is the Fermi velocity of massless Dirac fermions, δ (λ) is the MEC (Bychov-Rashba) energy scale, and $V(\mathbf{x})$ is a disorder potential describing impurity scattering. Here, $\{\boldsymbol{\tau}, \mathbf{\Sigma}, \mathbf{s}\}$ are Pauli matrices defined on valley, pseudospin, and spin spaces, respectively, and $\mathbf{p} = -i\mathbf{\nabla}$ is the 2D kinematic momentum operator for states near the K (K') point ($\tau_z = \pm 1$). This model describes magnetized graphene with C_{6v} point group symmetry [4,5] and can be easily extended to other ferromagnetic 2D materials such as $\mathrm{MoTe_2/EuO}$ [30–32]. We consider (nonmagnetic) matrix disorder with $V(\mathbf{x}) = \sum_i (u_0 1 + u_x\tau_x)\delta(\mathbf{x}-\mathbf{x}_i)$, where $\{\mathbf{x}_i\}_{i=1,\ldots,N}$ are random impurity positions and $u_{0(x)}$ parametrizes the intravalley (intervalley) scattering strength [33,34]. This choice allows us to interpolate between "smooth" potentials in clean samples ($|u_x| \ll |u_0|$) and the "sharp defect" limit of enhanced backscattering processes ($u_x \approx u_0$). The energy-momentum dispersion relation associated with clean system $H_0 = H - V(\mathbf{x})$ reads

$$\epsilon_{\mu\nu}(\mathbf{k}) = \mu\sqrt{v^2k^2 + M_\nu^2(k)}, \qquad (2)$$

where $M_\nu(k) = \sqrt{2\lambda^2 + \delta^2 + 2\nu\sqrt{\lambda^4 + v^2k^2(\lambda^2+\delta^2)}}$ is the SOC mass, and $k = |\mathbf{k}|$ is the wave vector measured from a Dirac point. Indices $\{\mu,\nu\} = \pm 1$ define the carrier polarity and the spin winding direction (Fig. 1). In the absence of SOC, the Dirac cones are shifted vertically, resulting in mixed electron-hole states near the Dirac point. For $\lambda \neq 0$, $\delta = 0$ (no MEC), the spectrum admits a spin-gap or "pseudogap" region, within which the spin and momentum of quasiparticles are locked at right angles (Bychov-Rashba spin texture) [15,35]. The combination of SOC and MEC opens a gap and splits the Dirac spectrum into three branches: regions I and III, defined by $|\lambda\delta|/\sqrt{\lambda^2+\delta^2} \equiv \epsilon_\mathrm{I} < |\epsilon| < \epsilon_\mathrm{II} = |\delta|$ and $|\epsilon| > \sqrt{4\lambda^2+\delta^2} \equiv \epsilon_\mathrm{III}$; those energy regimes are characterized by a nonsimply connected Fermi surface, allowing for scattering between states with different Fermi momenta; and region II, $\epsilon_\mathrm{II} < |\epsilon| < \epsilon_\mathrm{III}$ with only one band intersecting the Fermi level. For brevity, all functions are projected onto valley $\tau_z = 1$ (K point). The Bloch eigenstates read as

$$|\psi_{\mu\nu\mathbf{k}}(\mathbf{x})\rangle = \begin{pmatrix} e^{-\imath\phi_\mathbf{k}} \\ \imath\,\frac{(\epsilon_{\mu\nu}-\delta)^2 - v^2k^2}{2vk\lambda} \\ \frac{\epsilon_{\mu\nu}-\delta}{vk} \\ \imath\,\frac{(\epsilon_{\mu\nu}-\delta)^2 - v^2k^2}{2\lambda(\epsilon_{\mu\nu}+\delta)}\, e^{\imath\phi_\mathbf{k}} \end{pmatrix} e^{\imath\mathbf{k}\cdot\mathbf{x}}, \qquad (3)$$

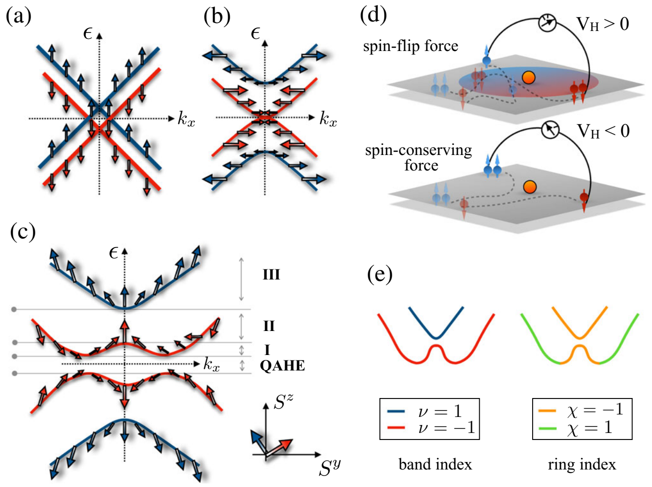

FIG. 1. (a)–(c) Energy bands and spin texture in systems with (a) MEC, (b) SOC, and (c) MEC and SOC. For visualization purposes, the bands are plotted along $\hat{k}_x$ (spins lie only in the yz plane). (d) Behavior of Hall conductivity due to competing spin-Lorentz forces. The elastic scattering channel dominates in regime II and III. (e) Band classification using band (ring) index $\nu = \pm 1$ ($\chi = \pm 1$).

where $\phi_\mathbf{k}$ is the wave vector polar angle. The noncoplanar spin texture in momentum space highlights the competition between different interactions: while the Bychov-Rashba effect favors in-plane alignment, the exchange interaction tilts the spins out of the plane, leading to a noncoplanar band polarization [Fig. 1(c)]. The pronounced effects of symmetry breaking on the spin texture has been highlighted in other systems, e.g., surface states of Bi thin films [36]. We underline here its impact on relativistic transport: as shown below, the out-of-plane spin texture $S^z_{\mu\nu\mathbf{k}} \equiv \frac{1}{2}\langle s_z\rangle_{\mu\nu\mathbf{k}}$ modulates intrinsic and extrinsic transport contributions; even if the electronic states are not fully spin polarized, it will prove useful to refer to *effective* spin-up ($S^z > 0$) and spin-down ($S^z < 0$) states. We focus on positive energies, $\epsilon > 0$, and also $\lambda, \delta > 0$, thus fixing $\mu = 1$ and omitting this index from the expressions.

Spin texture-driven skew scattering.—To assess the dominant extrinsic transport contributions in the metallic regime ($\epsilon > \epsilon_\mathrm{I}$), we solve the Boltzmann transport equations (BTEs) for a spatially homogeneous system. The formalism allows for the inclusion of a nonquantizing magnetic field and, more important, for a transparent physical interpretation of the scattering processes. For a controlled quantum diagrammatic treatment at the T-matrix level, we refer the reader to the Supplemental Material [37], where quantum side jump corrections are shown to be subleading for typical (dilute) impurity concentrations. The BTEs read as

$$\partial_t f_{\mathbf{k}_\chi} - e(\boldsymbol{\mathcal{E}} + \mathbf{v}\times\boldsymbol{\mathcal{B}})\cdot\nabla_\mathbf{k} f_{\mathbf{k}_\chi} = 2\pi n_i \sum_{\chi'=\pm1}\int \frac{Sd^2\mathbf{k}'}{(2\pi)^2}\left(f_{\mathbf{k}'_{\chi'}}\mathcal{T}_{\mathbf{k}'_{\chi'}\mathbf{k}_\chi} - f_{\mathbf{k}_\chi}\mathcal{T}_{\mathbf{k}_\chi\mathbf{k}'_{\chi'}}\right)\delta(\epsilon_{\mathbf{k}_\chi} - \epsilon_{\mathbf{k}'_{\chi'}}), \qquad (4)$$

where $f_{\mathbf{k}_\chi} = f^0_{\mathbf{k}_\chi} + \delta f_{\mathbf{k}_\chi}$ is the sum of the Fermi-Dirac distribution function and $\delta f_{\mathbf{k}_\chi}$, the deviation from equilibrium. Moreover, $\boldsymbol{\mathcal{E}}$ and $\boldsymbol{\mathcal{B}}$ are external dc fields, e is the elementary charge, and S is the area. The right-hand side is the collision term describing single impurity scattering and n_i is the impurity areal density. Subscripts $\chi, \chi' = \pm 1$ are "ring" indices for the outer or inner Fermi surfaces associated with momenta $k_\pm = v^{-1}\{\epsilon^2 + \delta^2 \pm [\epsilon^2\lambda^2 + (\epsilon^2 - \lambda^2)\delta^2]^{1/2}\}^{1/2}$ [Fig. 1(d)] [44]. Accounting for possible scattering resonances due to the Dirac spectrum [18], transition rates are evaluated by means of the T-matrix approach, i.e., $\mathcal{T}_{\mathbf{k}\mathbf{k}'} = |\langle \mathbf{k}'|t|\mathbf{k}\rangle|^2$, where $t = \mathcal{V}/(1 - g_0\mathcal{V})$ with $\mathcal{V} = u_0 + \tau_x u_x$ and $g_0 = \int d^2\mathbf{k}/(4\pi^2)(\epsilon - H_{0\mathbf{k}} + \imath 0^+)^{-1}$ is the integrated propagator. We start by considering $u_x = 0$, for which electrons undergo intra- and inter-ring scattering processes in the same valley (see the Supplemental Material [37] for a graphical visualization). Exploiting the Fermi surface isotropy, and momentarily setting $\boldsymbol{\mathcal{B}} = 0$, the exact solution to the linearized BTEs ($\nabla_{\mathbf{k}} f_{\mathbf{k}_\chi} \to \nabla_{\mathbf{k}} f^0_{\mathbf{k}_\chi}$) is

$$\delta f_{\mathbf{k}_\chi} = -e\left(\frac{\partial f^0_{\mathbf{k}_\chi}}{\partial \epsilon}\right)\mathbf{v}_{\mathbf{k}_\chi} \cdot (\tau^{\parallel}_\chi \boldsymbol{\mathcal{E}} + \tau^{\perp}_\chi \hat{z} \times \boldsymbol{\mathcal{E}}), \tag{5}$$

with $\mathbf{v}_{\mathbf{k}_\chi} = \nabla_{\mathbf{k}} \epsilon_\chi(\mathbf{k})$. In the above, $\tau^\varsigma_\chi = \tau^\varsigma_\chi(\epsilon, \lambda, \delta, u_0, n_i)$ are the longitudinal ($\varsigma = \|$) and transverse ($\varsigma = \perp$) transport times, given by

$$\boldsymbol{\tau}^{\|} = -2(\hat{\Lambda} + \hat{\Upsilon}\hat{\Lambda}^{-1}\hat{\Upsilon})^{-1}\mathbf{1}, \qquad \boldsymbol{\tau}^{\perp} = \hat{\Lambda}^{-1}\hat{\Upsilon}\boldsymbol{\tau}^{\|}, \tag{6}$$

where $\boldsymbol{\tau}^\varsigma = (\tau^\varsigma_\chi, \tau^\varsigma_{\bar{\chi}})^t$, $\hat{\Lambda} = ((\Lambda^-_\chi, \Lambda^+_\chi)^t, (\Lambda^-_{\bar{\chi}}, -\Lambda^+_{\bar{\chi}})^t)$, $\mathbf{1} = (1, 0)^t$, and $\bar{\chi} = -\chi$ ($\hat{\Upsilon}$ is obtained from $\hat{\Lambda}$ via the substitution $\Lambda^\pm_\chi \to \Upsilon^\mp_\chi$). The kernels $\Lambda^\pm_\chi$ and $\Upsilon^\mp_\chi$ are cumbersome functions of symmetric and skew cross sections defined by $\boldsymbol{\Gamma}_{\chi\chi'} = (n_i/2\pi)\int S d^2\mathbf{k}' \mathcal{T}_{\mathbf{k}'_{\chi'}\mathbf{k}_\chi}\{1, \cos\phi, \sin\phi\}^t$, with $\phi = \phi_{\mathbf{k}'} - \phi_{\mathbf{k}}$ [37]. Considering the two valleys, the general solution involves 16 cross sections. The exact form of the kernels is essential to correctly determine the energy dependence of the conductivity tensor. As shown in the Supplemental Material [37], including a magnetic field $\boldsymbol{\mathcal{B}} = \mathcal{B}\hat{z}$ only requires the substitution $\Gamma^{\sin}_{\chi\chi} \to \Gamma^{\sin}_{\chi\chi} + \omega_\chi$, where $\omega_\chi = k_\chi v_\chi^{-1}\mathcal{B}$ is the cyclotron frequency associated with the ring states. At $T = 0$, accounting for the valley degeneracy, we obtain the transverse response functions

$$\sigma^{c,s}_\perp(\mathcal{B}, \epsilon) = \frac{-e}{h}\sum_{\chi=\pm 1} k_\chi(\epsilon)\langle J_{c,s}(\epsilon)\rangle_\chi \tau^\perp_\chi(\epsilon, \mathcal{B}), \tag{7}$$

where $\langle J_{\{c,s\}}(\epsilon)\rangle_\chi = -e\langle\{1, s_z/2\}\boldsymbol{\Sigma} \cdot |\hat{z} \times \hat{\boldsymbol{\mathcal{E}}}|\rangle_\chi$ denotes the equilibrium transverse charge (spin) current of plane-wave states in the χ ring. The skew cross sections (and hence $\tau^\perp_\chi$) are found to be nonzero (except for isolated points) and thus, in the dilute regime, one has $\sigma^{c,s}_\perp \propto n_i^{-1}$, which is a signature of skew scattering [20]. As discussed below, the energy dependence of the skew cross sections is very marked, reflecting the out-of-plane spin texture of conducting electrons. For simplicity, in what follows, we work at saturation field $\mathcal{B} \geq \mathcal{B}_{\mathrm{sat}}$ such that the transverse responses coincide with their "anomalous" parts, that is, $\sigma_{\mathrm{AH(SH)}}(\mathcal{B}_{\mathrm{sat}}, \epsilon)|_\delta \simeq \sigma_\perp(0, \epsilon)|_{\delta_{\mathrm{sat}}}$, where $\delta_{\mathrm{sat}} = \delta[M_z(\mathcal{B}_{\mathrm{sat}})]$ and M_z is the magnetization.

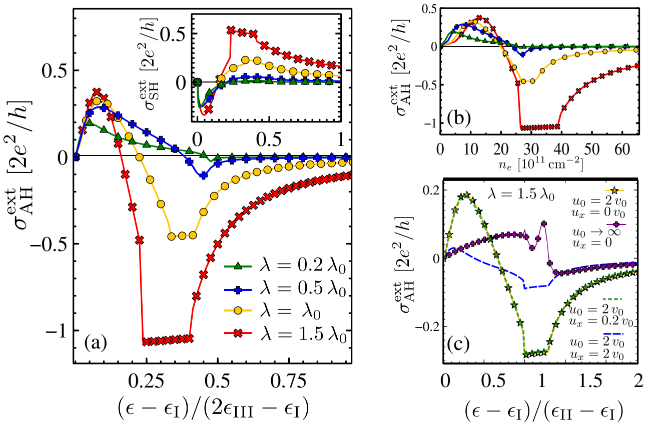

FIG. 2. Energy dependence of AHE and SHE. (a) $\sigma^{c,s}_\perp(\epsilon)$ is the result of the competing effective spin-Lorentz forces as discussed in the main text [see also Fig. 1(e)]. The change of sign is more prominent for large SOC. (b) $\sigma^c_\perp(n_e)$, where $n_e = \pi\{k_+^2 - k_-^2, k_+^2, k_+^2 + k_-^2\}$, respectively, in regions I–III. (c) While less evident in the unitary limit, the change of sign is robust across all scattering regimes. $\delta = 30$ meV, $\lambda_0 = \delta/3$, $v_0 = u_0 = 1$ eV nm^2, $u_x = 0$, and $n_0 = 10^{12}$ cm^{-2}.

The change of sign.—Focusing on the regime $\lambda \lesssim \delta$, we show how, approaching low carrier density, electrons undergoing spin-conserving and spin-flip scattering processes determine a change of sign in $\sigma^{c,s}_\perp$. For the sake of illustration, we assume weak scatterers $|g_0 u_0| \ll 1$ and restrict the analysis to intraring transitions within the outer ring: $\mathbf{k}_+ \to \mathbf{k}'_+$ (see additional discussions [37]). A first scenario for the change of sign is as follows. First, we note that as k is increased from $k = 0$, electron states in the lower band $\nu = -1$ progressively change their spin orientation from effective spin-up to spin-down states (see Fig. 1). Starting from ϵ_{I}, varying ϵ instead, it can be verified that the same occurs within the outer ring, such that by tuning ϵ one can switch between states with opposite spin polarization. As effective up and down states are associated with an opposite effective spin-Lorentz force (i.e., skew cross sections with opposite signs), this also means conducting electrons can be selectively deflected towards opposite boundaries of the system. The associated anomalous Hall (AH) voltage and SHE spin accumulation will then display the characteristic change of sign [Fig. 2(a)].

A second scenario involves the spin-flip force and does not require changing the polarization of carriers. Instead,

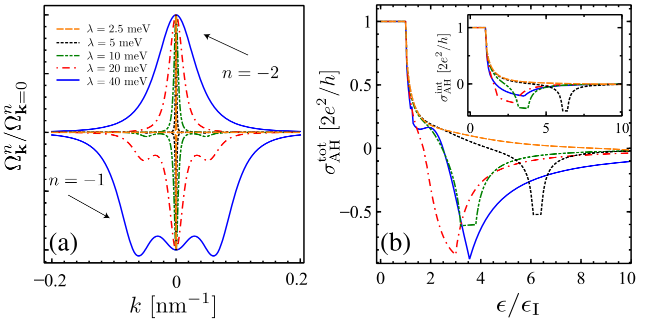

FIG. 3. Intrinsic contribution and total AH conductivity. (a) The Berry curvatures of hole bands $n = -1, -2$. Note that $\Omega_{n=-1}(\mathbf{k})$ develops additional "hot spots" as SOC is increased. (b) The total $\sigma^{\rm tot}_{\perp} = \sigma_{\perp} + \sigma^{\rm int}_{\perp}$ at selected values of λ; same legend as in (a). (b) Adding the intrinsic contribution (inset) to $\sigma_{\perp}$ leaves the estimate for ϵ_0 [Eq. (8)] virtually unaffected. Parameters: $u_0 = 10$ eV nm^2, $n_i = 10^{12}$ cm^{-2}, and $\delta = 30$ meV.

what changes when varying ϵ is the ratio of spin-flip to elastic skew cross sections. This also produces a change of sign as depicted in Fig. 1(e); the fate of the transverse conductivity will depend ultimately on the competition between the two effective spin-Lorentz forces (see the Supplemental Material [37]). The change of sign in $\sigma^{c,s}_{\perp}$ is a persistent feature as long as SOC and MEC are comparable [Fig. 2(a)]. In that case, the noncollinear spin texture is well developed, such that, on one hand, it is possible to interchange between effective spin-up and spin-down states "$S = \uparrow,\ \downarrow = -\bar{S}$" using a gate voltage, and on the other, both spin-conserving "$\langle S|V(\mathbf{x})|S\rangle$" and spin-flip "$\langle \bar{S}|V(\mathbf{x})|S\rangle$" scattering matrix elements are nonzero. Asymptotically, $\epsilon \gg \delta,\ \lambda$, the AH signal must vanish due to the opposite spin orientation of electron states belonging to $\nu = \pm 1$ bands, which produce vanishing small total magnetization $S^z(\epsilon) = \sum_{\chi} S^z_{\chi} \ll 1$. In comparison, the staggered field experienced by charge carriers $S^z_{\rm stag}(\epsilon) = \sum_{\chi} \chi S^z_{\chi}$ has slower asymptotic decay (for $\lambda \lesssim \delta$), implying that the SHE is more robust than the AHE.

Approaching the QAHE.—The system realizes the QAHE, provided the gap remains robust against disorder, $\sigma^c_{\perp}(\epsilon < \epsilon_{\rm I}) = 2e^2/h$, $\sigma^s_{\perp}(\epsilon < \epsilon_{\rm I}) = 0$. In the metallic regime, the Berry curvature of occupied states also provide a (nonquantized) intrinsic contribution to the transverse conductivity. Below, we discuss how robust is the change of sign to the inclusion of other factors and also how the quantized region is approached. First, consider that, in the strong scattering limit $|g_0 u_0| \gg 1$, the rate of inter-ring transitions increases and the one-ring scenario presented above might break down. However, as shown in Fig. 2(c) the change of sign is still visible. In real samples, structural defects and short-range impurities, such as hydrocarbons [45], induce scattering between inequivalent valleys, thereby opening the backscattering channel [34]. In fact, spin precession measurements in graphene with interface-induced SOC indicate that the in-plane spin dynamics is sensitive to intervalley scattering [46–48]. To determine the impact of intervalley processes on dc transport, we solved the BTEs for arbitrary ratio u_x/u_0. Figure 2(c) shows the AH conductivity for selected values of u_x (dashed lines). $\sigma^c_{\perp}$ is strongly impacted, showing a 50% reduction when intra- and intervalley scattering processes are equally probable ($u_x = u_0$). However, the sign change in $\sigma_{\perp}$, approaching the majority spin band edge $\epsilon \approx \epsilon_{\rm II}$, is still clearly visible. Further analysis is given in the Supplemental Material [37], where we also analyze the impact of thermal fluctuations, concluding that the features described above are persistent up to $k_B T \approx k_B T_{\rm room}/2 \simeq 12$ meV for $\lambda \approx \delta = 30$ meV. A thorough numerical analysis in the strong SOC regime provides an estimation for ϵ_0, defined as $\sigma_{\perp}(\epsilon_0) = 0$,

$$\epsilon_0 = a\epsilon_{\rm I} + b\epsilon_{\rm III}, \tag{8}$$

with $a \simeq 0.3$–0.4 and $b \simeq 0.6$–0.8. This relation shows that the knowledge of δ (e.g., from the Curie temperature [4]) allows us to estimate the SOC strength directly from the gate voltage dependence of the AH resistance. The values $\sigma_{\perp} \approx 0.1$–$1$ (e^2/h) are compatible with the measurements in Refs. [4,5], for a reasonable choice of parameters, $0 \leq \lambda$, $\delta \leq 30$ meV in the dirty regime with $n_i = 10^{12}$ cm^2 and $u_0 \sim (0.1, 1)$ eV nm^2. In high-mobility samples, our theory predicts that the robust skew scattering contribution with $\sigma_{\perp} \propto n_i^{-1}$ results in much larger values $\sigma_{\perp} \approx 10$–$100$ (e^2/h).

Intrinsic contribution and total AH conductivity.—We now report our results for the intrinsic contribution. Previous studies—where the topological nature of the model was also first pointed out [11]—tackled the problem numerically, also with a focus on the regime $\delta \gg \lambda$. We go beyond this limitation, performing an exact analytic evaluation of the intrinsic AH conductivity. Starting from the chiral eigenstates of Eq. (3), we obtain the Berry curvature of the bands as $\Omega^n_{\mathbf{k}} = (\nabla_{\mathbf{k}} \times \boldsymbol{\mathcal{A}}^n_{\mathbf{k}})_z$, where $\boldsymbol{\mathcal{A}}^n_{\mathbf{k}} = -i\langle n\mathbf{k}|\nabla_{\mathbf{k}}|n\mathbf{k}\rangle$ and $n \equiv (\mu, \nu)$ is a combined band index [49]. The transverse conductivity is obtained via integration of the Berry curvatures [50], $\sigma^{\rm int}_{\perp} = \sum_n \sum_{\mathbf{k}} \Omega^n_{\mathbf{k}} f^0_{k_n}$. Note that $\sum_n \Omega^n_{\mathbf{k}} = 0$ and $\sum_{\mathbf{k}} \sum_{n<0} \Omega^n_{\mathbf{k}} = 2e^2/h$, which is the case when ϵ is tuned into the gap. The full form of $\boldsymbol{\mathcal{A}}^n_{\mathbf{k}}$ is reported in Ref. [37], where we also show that the intrinsic contribution can be equivalently obtained from the clean limit of the Kubo-Streda formula. The result is plotted in the inset of Fig. 3(b), while Fig. 3(a) shows the opposite-in-sign Berry curvatures for the bands $n = -1$ and -2. Similar to the situation presented for the extrinsic contribution, we find the intrinsic term also presents a peculiar change of sign under the same condition $\lambda > \lambda_c \approx \delta/6$ [see Fig. 2(a)], where λ_c is a critical value for the Bychov-Rashba strength. The effect in this case is ascribed to the profile of the Berry curvatures; in particular, in the electron sector, the change of sign happens for $\epsilon = \tilde{\epsilon}_0$ solution of the self-consistent equation

$$I_1|_{k_-}^{k_+}(\tilde{\epsilon}_0) + \theta_{\tilde{\epsilon}_0,\epsilon_{\mathrm{II}}} I_1|_0^{k_+}(\tilde{\epsilon}_0) + \theta_{\tilde{\epsilon}_0,\epsilon_{\mathrm{III}}} I_2|_0^{k_-}(\tilde{\epsilon}_0) = -\frac{2e^2}{h}, \quad (9)$$

where $I_i|_a^b(\epsilon) \equiv \int_{a(\epsilon)}^{b(\epsilon)} dkk\Omega_{\mathbf{k}}^i$ and $\theta_{\epsilon_a,\epsilon_b} = \theta(\epsilon_a - \epsilon_b)$ is the Heaviside step function. In Fig. 3(b), we show the total AH conductivity, given by $\sigma_\perp^{\mathrm{tot}} = \sigma_\perp^{\mathrm{int}} + \sigma_\perp^c$. Remarkably, we find $\tilde{\epsilon}_0 \simeq \epsilon_0$, such that our estimate for the AHE reversal energy (ϵ_0) in Eq. (8) is still accurate when all contributions are added [cf. Fig. 3(b) and inset]. This robust energy dependence in the AHE and SHE transverse response functions connects the skew scattering mechanism, unveiled in this work, to the intrinsic properties of magnetized 2D Dirac bands.

No new data were collected in the course of this research.

The authors are grateful to Denis Kochan, Chunli Huang, and Mirco Milletarì for useful discussions. We thank Stuart Alan Cavill and Roberto Raimondi for critically reading the manuscript and for helpful comments. A. F. gratefully acknowledges the financial support from the Royal Society (U.K.) through a Royal Society University Research Fellowship. M. O. and A. F. acknowledge funding from EPSRC (Grant No. EP/N004817/1).

---

[*] aires.ferreira@york.ac.uk

[1] C. Gong *et al.*, Nature (London) **546**, 265 (2017).

[2] B. Huang *et al.*, Nature (London) **546**, 270 (2017).

[3] A. G. Swartz, P. M. Odenthal, Y. Hao, R. S. Ruoff, and R. K. Kawakami, ACS Nano **6**, 10063 (2012).

[4] Z. Wang, C. Tang, R. Sachs, Y. Barlas, and J. Shi, Phys. Rev. Lett. **114**, 016603 (2015).

[5] C. Tang, B. Cheng, M. Aldosary, Z. Wang, Z. Jiang, K. Watanabe, T. Taniguchi, M. Bockrath, and J. Shi, APL Mater. **6**, 026401 (2018).

[6] J. C. Leutenantsmeyer, A. A. Kaverzin, M. Wojtaszek, and B. J. van Wees, 2D Mater. **4**, 014001 (2017).

[7] P. Wei *et al.*, Nat. Mater. **15**, 711 (2016).

[8] Y. F. Wu *et al.*, Phys. Rev. B **95**, 195426 (2017).

[9] D. Zhong *et al.*, Sci. Adv. **3**, e1603113 (2017).

[10] H. Haugen, D. Huertas-Hernando, and A. Brataas, Phys. Rev. B **77**, 115406 (2008).

[11] Z. Qiao, S. A. Yang, W. Feng, W.-K. Tse, J. Ding, Y. Yao, J. Wang, and Q. Niu, Phys. Rev. B **82**, 161414(R) (2010).

[12] Q. F. Sun, Z. T. Jiang, Y. Yu, and X. C. Xie, Phys. Rev. B **84**, 214501 (2011).

[13] H. X. Yang, A. Hallal, D. Terrade, X. Waintal, S. Roche, and M. Chshiev, Phys. Rev. Lett. **110**, 046603 (2013).

[14] D. Marchenko, A. Varykhalov, J. Sanchez-Barriga, O. Rader, C. Carbone, and G. Bihlmayer, Phys. Rev. B **91**, 235431 (2015).

[15] E. I. Rashba, Phys. Rev. B **79**, 161409 (2009).

[16] T.-W. Chen, Z.-R. Xiao, D.-Wei Chiou, and G.-Y. Guo, Phys. Rev. B **84**, 165453 (2011).

[17] Z. Qiao, H. Jiang, X. Li, Y. Yao, and Q. Niu, Phys. Rev. B **85**, 115439 (2012); Z. Qiao, W. Ren, H. Chen, L. Bellaiche, Z. Zhang, A. H. MacDonald, and Q. Niu, Phys. Rev. Lett. **112**, 116404 (2014); J. Zhang, B. Zhao, Y. Yao, and Z. Yang, Phys. Rev. B **92**, 165418 (2015).

[18] A. Ferreira, T. G. Rappoport, M. A. Cazalilla, and A. H. Castro Neto, Phys. Rev. Lett. **112**, 066601 (2014).

[19] D. V. Tuan, J. M. Marmolejo-Tejada, X. Waintal, B. K. Nikolić, S. O. Valenzuela, and S. Roche, Phys. Rev. Lett. **117**, 176602 (2016).

[20] M. Milletarì and A. Ferreira, Phys. Rev. B **94**, 134202 (2016); M. Milletarì and A. Ferreira, Phys. Rev. B **94**, 201402(R) (2016).

[21] C. Huang, Y. D. Chong, and M. A. Cazalilla, Phys. Rev. B **94**, 085414 (2016).

[22] K. Zollner, M. Gmitra, T. Frank, and J. Fabian, Phys. Rev. B **94**, 155441 (2016).

[23] M. Gmitra, D. Kochan, P. Hogl, and J. Fabian, Phys. Rev. B **93**, 155104 (2016).

[24] Z. Wang, D.-K. Ki, H. Chen, H. Berger, A. H. MacDonald, and A. F. Morpurgo, Nat. Commun. **6**, 8339 (2015).

[25] J. C. Leutenantsmeyer, A. A. Kaverzin, M. Wojtaszek, and B. J. van Wees, 2D Mater. **4**, 014001 (2017).

[26] J. Sinova, S. O. Valenzuela, J. Wunderlich, C. H. Back, and T. Jungwirth, Rev. Mod. Phys. **87**, 1213 (2015).

[27] B. F. Miao, S. Y. Huang, D. Qu, and C. L. Chien, Phys. Rev. Lett. **111**, 066602 (2013).

[28] K. S. Das, W. Y. Schoemaker, B. J. van Wees, and I. J. Vera-Marun, Phys. Rev. B **96**, 220408(R) (2017).

[29] S. Iihama, Y. Otani, and S. Maekawa, National electronics review **1**, 120 (2018).

[30] J. Qi, X. Li, Q. Niu, and J. Feng, Phys. Rev. B **92**, 121403 (R) (2015).

[31] C. Cheng, J.-T. Sun, X.-R. Chen, H.-X. Fua, and S. Meng, Nanoscale **8**, 17854 (2016).

[32] Q.-F. Yao, J. Cai, W.-Y. Tong, S.-J. Gong, J.-Q. Wang, X. Wan, C.-G. Duan, and J. H. Chu, Phys. Rev. B **95**, 165401 (2017).

[33] A. Ferreira, J. Viana-Gomes, J. Nilsson, E. R. Mucciolo, N. M. R. Peres, and A. H. Castro Neto, Phys. Rev. B **83**, 165402 (2011).

[34] N. M. R. Peres, Rev. Mod. Phys. **82**, 2673 (2010).

[35] M. Offidani, M. Milletarì, R. Raimondi, and A. Ferreira, Phys. Rev. Lett. **119**, 196801 (2017).

[36] A. Takayama, T. Sato, S. Souma, and T. Takahashi, Phys. Rev. Lett. **106**, 166401 (2011).

[37] See the Supplemental Material at http://link.aps.org/supplemental/10.1103/PhysRevLett.121.126802 for derivations and additional calculations, including the quantum side jump correction and the analytical form of the Berry curvature in the full model, which also includes Refs. [20,38–43].

[38] D. M. Basko, Phys. Rev. B **78**, 115432 (2008).

[39] A. Pachoud, A. Ferreira, B. Özyilmaz, and A. H. Castro Neto, Phys. Rev. B **90**, 035444 (2014).

[40] P. Streda, J. Phys. C **15**, L1299 (1982).

[41] A. Crepieux and P. Bruno, Phys. Rev. B **64**, 014416 (2001).

[42] N. A. Sinitsyn, A. H. MacDonald, T. Jungwirth, V. K. Dugaev, and J. Sinova, Phys. Rev. B **75**, 045315 (2007).

[43] I. A. Ado, I. A. Dmitriev, P. M. Ostrovsky, and M. Titov, Europhys. Lett. **111**, 37004 (2015).

[44] In region I, the states $|\mathbf{k}_{\pm}\rangle$ belong to the same Bloch band $\nu = -1$, whereas in region III they populate the $\nu = \pm 1$ bands. In region II, the only populated state (ring $\chi = 1$) coincides with the Bloch eigenstate $|\psi_{\mu=1,\nu=-1\mathbf{k}}(\mathbf{x})\rangle$.

[45] Z. H. Ni *et al.*, Nano Lett. **10**, 3868 (2010).

[46] L. A. Benítez, J. F. Sierra, W. S. Torres, A. Arrighi, F. Bonell, M. V. Costache, and S. O. Valenzuela, Nat. Phys. **14**, 303 (2018).

[47] A. W. Cummings, J. H. García, J. Fabian, and S. Roche, Phys. Rev. Lett. **119**, 206601 (2017).

[48] T. S. Ghiasi, J. I. Aynés, A. A. Kaverzin, and B. J. van Wees, Nano Lett. **17**, 7528 (2017).

[49] We assign the label n in descending order, starting from the band of highest energy. Thus, $\nu, \mu = \pm(1,1) \rightarrow n = \pm 2$ and $\nu, \mu = \pm(1,-1) \rightarrow n = \pm 1$.

[50] D. J. Thouless, M. Kohmoto, M. P. Nightingale, and M. den Nijs, Phys. Rev. Lett. **49**, 405 (1982); N. Nagaosa, J. Sinova, S. Onoda, A. H. MacDonald, and N. P. Ong, Rev. Mod. Phys. **82**, 1539 (2010); F. D. M. Haldane, Rev. Mod. Phys. **89**, 040502 (2017).